JOURNAL OF MATERIALS RESEARCH AND TECHNOLOGY 2022;18:3319–3335

Available online at www.sciencedirect.com

jmr&t Journal of Materials Research and Technology

journal homepage: www.elsevier.com/locate/jmrt

Original Article

The role of the g-C_3N_4 precursor on the P doping using HCCP as a source of phosphorus

Vlastimil Matějka [a,b,*], *Radim Škuta* [a,b], *Kryštof Foniok* [a], *Vlastimil Novák* [c], *Daniel Cvejn* [b,d], *Alexandr Martaus* [b], *Monika Michalska* [a], *Jiří Pavlovský* [a], *Petr Praus* [a,b]

[a] *Department of Chemistry, Faculty of Materials Science and Technology, VSB - Technical University of Ostrava, 17. Listopadu 2172/15, 708 00, Ostrava-Poruba, Czech Republic*

[b] *Institute of Environmental Technology, CEET, VSB - Technical University of Ostrava, 17. Listopadu 2172/15, 708 00, Ostrava-Poruba, Czech Republic*

[c] *Department of Physical Chemistry and Theory of Technological Processes, Faculty of Materials Science and Technology, VSB - Technical University of Ostrava, 17. Listopadu 2172/15, 708 00, Ostrava-Poruba, Czech Republic*

[d] *ENET Centre, CEET, VSB - Technical University of Ostrava, 17. Listopadu 2172/15, 708 00, Ostrava-Poruba, Czech Republic*

ARTICLE INFO

Article history:
Received 13 January 2022
Accepted 3 April 2022
Available online 7 April 2022

Keywords:
Graphitic carbon nitride
Phosphorus doping
Hexachlorocyclotriphosphazene
Photocatalysis

ABSTRACT

This work describes the doping of graphitic carbon nitride (g-C_3N_4) with phosphorus performed by 2-h heat treatment of a mechanical mixture of g-C_3N_4 precursor (urea, dicyandiamide, and guanidine hydrochloride) with hexachlorocyclotriphosphazene at 525 °C. The amount of fixed phosphorus in the resulting g-C_3N_4 structure reached approximately 10 wt% in the case of the urea precursor. For the other two precursors, the fixed phosphorus content in the final products was less than 5 wt%. Several experimental techniques (SEM, XRFS, TG, XRD, FTIR, physisorption of nitrogen, UV-VIS DRS, PL spectroscopy, and electrochemical analysis) were used to characterize the prepared samples. The photodegradation activity of the samples was determined by degradation of Rhodamine B under irradiation with visible light (420 nm). In general, the photodegradation activity of the samples was dependent on the phosphorus content. The highest photodegradation activity was obtained for urea-based g-C_3N_4 doped with the lowest phosphorus content, with a threefold increase in calcination product yield. The mechanism of incorporation of phosphorus into the final g-C_3N_4 structure was explained as a two-phase process.

* Corresponding author.
E-mail address: vlastimil.matejka@vsb.cz (V. Matějka).

https://doi.org/10.1016/j.jmrt.2022.04.019

1. Introduction

Graphitic carbon nitride is a well-known and widely studied semiconductor [1–4] with various possible applications. For instance, it can be used in photocatalysis [5–7], sensors [8,9], hydrogen production [10–12], batteries, supercapacitors [13,14], and many more [15–18]. Regarding photocatalytic applications, the main advantages of g-C_3N_4 include chemical, photochemical, and thermal stability, non-toxicity, and most importantly, low cost and ease of preparation. The narrower band gap energy (around 2.7 eV) compared to TiO_2 (3.2 eV) enables g-C_3N_4 to absorb VIS irradiation and thus significantly increase the efficiency of light-harvesting for applications based on photocatalytic processes.

The frequently used procedure for preparing g-C_3N_4 is the thermal polymerization of a suitable nitrogen-rich precursor heated in a semi-closed crucible, typically at temperatures in the range of 500–600 °C. The g-C_3N_4 precursor that has received the most attention is undoubtedly melamine [19–22]. Other precursors are urea [23–25], dicyandiamide [26,27], guanidine [28,29], and ionic liquids, such as 1-butyl-3-methylimidazolium hexafluorophosphate, which are beneficial as phosphorus sources [30]. However, g-C_3N_4 samples prepared in this way usually suffer from low specific surface area and fast electron-hole recombination, which impairs photocatalytic performance.

Therefore, several strategies have been adopted to improve g-C_3N_4 photocatalytic performance. Thermal, chemical, or mechanical exfoliation processes [31–36] are used to increase the specific surface area of g-C_3N_4. Various approaches such as doping g-C_3N_4 with metallic and nonmetallic elements [37–45], coupling with other semiconductors [46–50], inert matrices [51–53], or a combination of both [54,55] have been used to suppress the electron-hole recombination rate. Recently, the doping of g-C_3N_4 with non-metal elements has attracted attention, as it allows lowering of the band gap energy and tuning of the valence and conduction bands [40,56]. In addition, doping with phosphorus (P-doping) has been reported to be efficient in improving photocatalytic activity [29,57,58]. Li et al. [59] modified g-C_3N_4 by phosphorus and boron to weaken van der Waals interactions between individual layers of g-C_3N_4. The resulting material, ultrathin co-doped g-C_3N_4 nanosheets, exhibited a high potential for hydrogen production. Regarding P-doping, it is noteworthy to mention frequently used precursors, in particular, inexpensive ammonium hydrogenphosphate [60,61], phytic or phosphoric acids [62,63], 2-aminoethylphosphonic acid [64] and hexachlorocyclotriphosphazene (HCCP) [65,66].

Our group has recently reported *in situ* P-doping of g-C_3N_4 using the mixtures of melamine and HCCP [67]. In addition to promising catalytic activities, the resulting materials showed interesting structural differences compared to pristine and other P-doped g-C_3N_4. It was demonstrated that the presence of HCCP affects not only the structure of the final material but also the nature of the P-doping. Also, a doping mechanism was proposed, including the indication of possible phosphorus positions in the polymeric structure of g-C_3N_4.

In this work, we follow up on our previous study [67] and expand the group of g-C_3N_4 precursors to include urea, dicyandiamide, and guanidine hydrochloride. The samples were prepared by a one-pot thermal polymerization procedure and further characterized using the methods of physico-chemical and phase analysis. The photocatalytic performance of the prepared samples was evaluated by the visible light induced photodegradation of Rhodamine B.

2. Materials and methods

2.1. Chemicals

All of the chemicals used were purchased from companies listed below in reagent grade, analytical grade, or equivalent quality. Urea (UR) came from Carl Roth Co. GmBH (Germany), dicyandiamide (DCDA) was obtained from Merck KGaA (Germany), guanidine hydrochloride (GUA) was obtained from VWR LifeSciences (Czech Republic), hexachlorocyclotriphosphazene was obtained from Sigma Aldrich (USA), Rhodamine B (RhB) was obtained from Fisher Scientific (USA). The water used for the preparation of all solutions was deionized and prepared using reverse osmosis (Aqua Osmotic, Czech Republic).

2.2. Sample preparation

Phosphorus-modified graphitic carbon nitride was prepared according to our previous study [67] by the 2 h long thermal polymerization of a mechanical mixture of the given g-C_3N_4 (further labeled as CN) precursor (UR, DCDA, and GUA) and HCCP at 525 °C with a heating rate of 2 °C·min^{-1}. After this period of heating, the samples were allowed to cool down inside the furnace. The undoped CN was prepared by the same thermal treatment of pure precursors (UR, DCDA, and GUA).

For all calcination experiments, the initial mechanical mixture (5 g) containing the given CN precursor with 0, 1, 10, 20, 30, and 40 wt% of HCCP was placed in a semi-closed ceramic crucible and subjected to the heat treatment mentioned above. The sample labelling system is described in Table 1.

2.3. Characterization methods

2.3.1. X-ray powder diffraction

X-ray powder diffraction (XRD) patterns were measured using a SmartLab diffractometer (Rigaku, Japan), equipped with a detector D/teX Ultra 250. A cobalt tube (CoKα, $\alpha_1 = 0.178892$ nm, $\alpha_2 = 0.179278$ nm), operated at 40 mA and

Table 1 – Denotation of samples.

Temperature	Un-doped samples	P doped samples
UR	UR-CN	URx-PCN[a]
DCDA	DCDA-CN	DCDAx-PCN[a]
GUA	GUA-CN	GUAx-PCN[a]

[a] x - wt% of HCCP in the pyrolysis mixture (1, 10, 20, 30 and 40). As an example, the sample denoted as UR20-PCN was prepared by the calcination of urea + HCCP mechanical mixture with HCCP content of 20 wt%.

40 kV, was used as a radiation source. The powder samples were ground in an agate mortar, pressed using a microscope glass in a rotational sample holder, and measured in a reflection mode. The samples were rotated at constant speed of 15 rpm during measurement to eliminate the preferred orientation effect. XRD patterns were obtained in the 2 theta range of 5°–90° with a step size of 0.01° and the speed of $0.5^{\circ}min^{-1}$.

2.3.2. *Elemental analysis*

The content of C, N, and H was measured using a combustion method with a CHSN628 elemental analyser (Leco, USA). In a typical experiment, the powder sample (100 mg) was weighed in tin foil cups and transferred to a furnace by the autosampler.

2.3.3. *FTIR spectroscopy*

The Fourier transform infrared (FTIR) spectra of the prepared samples were measured using a Thermo Scientific Nicolet iS10 FTIR spectrometer (Thermo Scientific, USA). Measurements were carried out in the range of 500–4000 cm^{-1} with a resolution of 2 cm^{-1} using an attenuated total reflection (ATR) technique. Each spectrum obtained was the average of 64 scans. Before each measurement, the background was scanned to eliminate apparatus and environmental effects.

2.3.4. *X-ray fluorescence spectroscopy*

X-ray fluorescence spectroscopy (XRFS) was performed using an energy dispersive spectrometer Spectro XEPOS equipped with a 50 W Pd X-ray tube. The samples were inserted into a plastic cuvette sealed with a protective Mylar foil and subsequently analysed in the helium atmosphere.

2.3.5. *Scanning electron microscopy*

For microscopic investigations of the samples, a scanning electron microscope (SEM: Tescan Vega) with a tungsten cathode and energy-dispersive X-ray spectroscopy (EDS: EDAX) was used. The SEM micrographs were obtained using a secondary electrons (SE) and backscattered electrons (BSE) mode with an acceleration voltage of 30 kV. Before measurement, the samples were gold sputtered to ensure adequate electron conductivity.

2.3.6. *UV-VIS DRS spectroscopy*

UV-VIS diffusion reflectance spectra were obtained using a Shimadzu UV-2600 spectrometer (Shimadzu, Japan), equipped with an integrating sphere 2600 Plus. Pulverised samples were placed inside a holder, and the spectra were recorded at room temperature in the range of 200–900 nm. Extra pure barium sulphate powder was used for baseline registration. The Tauc plots were used to evaluate indirect band gap energies.

2.3.7. *Electrochemical testing*

Electrochemical testing was used to determine the VB and CB energies using Mott-Schottky approach. The electrochemical measurements were performed in three-electrode system using Autolab PGSTAT302 potentiometer (Metrohm). Glassy carbon electrode (GCE) (Metrohm), Ag/AgCl (3 M KCl) electrode (Metrohm), and Pt sheet (Metrohm) served as a working, reference, and counter electrode, respectively. For each of the experiment, the surface of GCE was coated with thin layer of tested sample by applying of 30 μl of water suspension of tested sample (10 mg of sample in 5 ml of deionized water) on a top of GCE tip. In following step, the coated GCE tip was dried at 85 °C for 30 min. The measurements were conducted in 0.1 M KCl electrolyte (pH = 5.8), and prior the measurement the electrolyte was purged with nitrogen for 30 min. All electrochemical performances were achieved at room temperature. For the measurement an AC signal having an amplitude of 10 mV and frequency 300 Hz was applied.

2.3.8. *Photoluminescence spectroscopy*

Emission PL spectra were acquired on a spectrometer FLSP920 series spectrometer (Edinburgh Instruments, Ltd.) equipped with a Xe900 arc non ozone lamp (450 W) and an R928P type detector (PMT detector). The excitation wavelength of 325 nm was used for all measurements.

2.3.9. *Specific surface area*

The specific surface area (SSA) of the samples was measured at 77 K under less than 1Pa vacuum using a Sorptomatic 1990 device (ThermoFinnigan, USA) with gaseous nitrogen as adsorbate. SSA values were calculated according to Brunauer – Emmett –Teller (BET) theory in the relative pressure range of 0.05–0.25.

2.3.10. *Thermal analysis*

Thermal gravimetry (TG) of the UR, DCDA, GUA and their mechanical mixtures with 20 wt% of HCCP were carried out using a Setaram SETSYS 18TM thermal analyser and an S-type measuring rod. Samples (10 mg) were placed in an alumina crucible covered with an alumina lid. The analysis was carried out in the dynamic atmosphere of argon (the flow rate of 1.5 $dm^3 h^{-1}$) with the heating rate of 10 $°C \cdot min^{-1}$ from 20 °C to 900 °C.

2.3.11. *Determination of the phosphate ions*

To determine the presence of nonbonded phosphate ions, the water suspensions of the synthesized samples (0.015 g in 50 cm^3 deionized water) were prepared and mixed for 2 h using an electromagnetic stirrer (250 rpm). After this period, suspensions were vacuum filtered through a membrane filtrate paper with porosity of 0.60 μm (Pragopor, Czech Republic). The concentration of phosphates was determined by VIS spectrometry using an internally validated molybdenum blue method. In our case, 30 cm^3 of a filtrate was taken into a 50 cm^3 volume flask and sulphuric acid (5.4 mol dm^{-3}), $(NH_4)_2Mo_7O_{24}.4H_2O$ and $(NH_4)_2Fe(SO_4)_2$ solutions, each of 5 cm^3 volume, were added. After 10 min leaving to stand, the colored solutions were poured into 2 cm optical length cuvettes and visible light absorbance ($\lambda = 700$ nm) was measured using a Helios β UV-VIS spectrophotometer (UNICAM).

2.3.12. *Photodegradation experiment*

The photocatalytic activity of selected CN and PCN samples was evaluated using the VIS assisted photodegradation of Rhodamine B (RhB) as the model compound in aqueous solution. A LED diode lamp with the maximum light intensity at 420 nm (the light intensity on the irradiated suspension surface was 7 mW cm^{-2}) was used for suspension irradiation.

In a typical photocatalytic procedure, 0.05 g of the pulverised sample was mixed with 165 cm^3 of the RhB solution with a concentration of 10 $mg \cdot dm^{-3}$. The prepared suspension was stirred at 250 rpm in darkness for 90 min to achieve absorption equilibrium. In the next step, the prepared suspension was stirred at 250 rpm under VIS irradiation for 90 min and 4 cm^3 of samples were taken in 15, 30, 60 and 90 min. The suspensions taken were filtered using a 0.45 mm pore size syringe filter (CHROMAFIL GF/RC-20/25 filters, Macherey-Nagel, Germany) to separate the CN material. The absorption spectra of the residual dye were measured using a UV-2600 spectrometer (Shimadzu, JP) in 1 cm quartz glass microcuvettes.

To understand RhB photodegradation, photodegradation tests were also performed in the presence of ethylenediaminetetraacetic acid (EDTA), 1,4 benzoquinone (1,4-BQ) and t-butanol (t-Bu) as scavengers of the holes (h^+), superoxide radicals ($\bullet O_2^-$) and hydroxyl radicals ($\bullet OH$).

3. Results and discussion

3.1. Yield of calcination

The yields of the calcination products for the given precursor and the amount of HCCP are compared in Fig. 1. The highest yields in the range of 42–65% were achieved for the DCDA precursor. Calcination of the mixtures of UR + HCCP and GUA + HCCP led to a significant decrease in the yield of the calcination product, reaching a maximum of 29 and 25% for GUA and UR, respectively. Compared to the previous study on melamine, where the yields ranged from 63% to 43% at 525 °C [67], the yields of CN prepared from guanidine and urea CN precursor are significantly lower. Even with such a high mass loss in the case of the UR precursor, visible evaporation of the gaseous products was not observed during heating of the respective mechanical mixtures.

Figure 1 also shows that the trends in the dependencies of product yields on HCCP content for GUA and DCDA are similar and show an almost constant value of up to 10 wt% of HCCP followed by its decrease with growing HCCP content. In the case of UR, Fig. 1 shows an increased tendency of the product yield up to 20 wt% of HCCP followed by its decrease with the HCCP content. Our previous research focused on the P-doping of CN prepared by the same calcination procedure applied to the mixture melamine + HCCP revealed a continuous decrease in product yield with the HCCP content [67]. When the trends in the yields are compared, DCDA and GUA behave similarly to UR. The product yield of g-C_3N_4 prepared from pure UR precursor (UR-CN) is the lowest, reaching only 3%. This indicates that urea is the least thermally stable precursor.

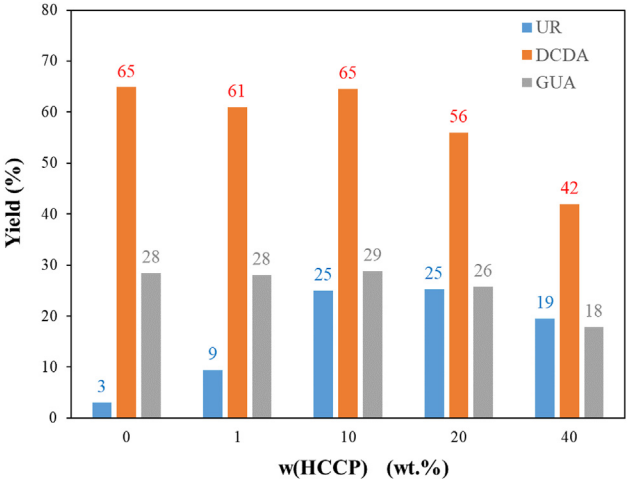

Fig. 1 – Yields of calcination based on HCCP content.

The presence of HCCP enhanced the overall yield of the CN synthesis. This effect is evident in the case of urea, when 1 wt % of HCCP in the reaction mixture triples the overall yield, and 10 wt% of HCCP in the reaction mixture increased the yield more than eight times. The content of HCCP up to 10 wt% in the reaction mixture appears to benefit the CN yield. This leads to the hypothesis that HCCP participated in the CN-forming reactions as a P-donor and an activating agent for CN precursors.

3.2. Scanning electron microscopy

The character of the CN (both pure and P-doped) particles synthesized using UR, DCDA, and GUA as the precursors are shown in Fig. 2 a)-f).

The obtained images indicate that the finest morphology was obtained for the sample UR-CN (Fig. 2a-b), while both samples (un-doped and P-doped) prepared from DCDA show a dense microstructure (Fig. 2c-d). Regarding the sample prepared with UR, the agglomeration effect of HCCP on the final sample UR-20HCCP is evident since the morphology of the UR-CN particles (Fig. 2a) shows a very fine microstructure compared to the particles synthesized using the mixture of UR+20wt% of HCCP (Fig. 2b). The GUA-CN sample shows the most organized microstructure (Fig. 2e), and the doping of this sample with phosphorus caused a slight disintegration of the particles (Fig. 2f). Comparing the images shown in Fig. 2a, c, and e, it is evident that the g-C_3N_4 precursor (UR, DCDA or GUA) is the main reason for the different morphologies of the final calcination products.

3.3. Elemental composition

The comparison of the theoretical amount of phosphorus (P_T) carried with the given amount of HCCP and the real amount of phosphorus determined using the XRFS technique ($P_{content}$) is shown in Table 2.

The results in Table 2 show that the real phosphorus content increased with increasing HCCP content and demonstrate that most of the samples had phosphorus yield higher than 100% ($P_{content}/P_T > 1$). This yield shows that the given CN precursor was intensively decomposed, while the HCCP-derived phosphorus remained in the final structure of the calcination products. This is in good agreement with the results presented in Fig. 1a, which showed the lowest yield of calcination products for UR.

However, for the samples DCDA1-PCN, DCDA20-PCN, DCDA40-PCN, and GUA40-PCN, the amount of captured phosphorus was lower than the theoretical one. These results also confirm the highest thermal stability of DCDA and the

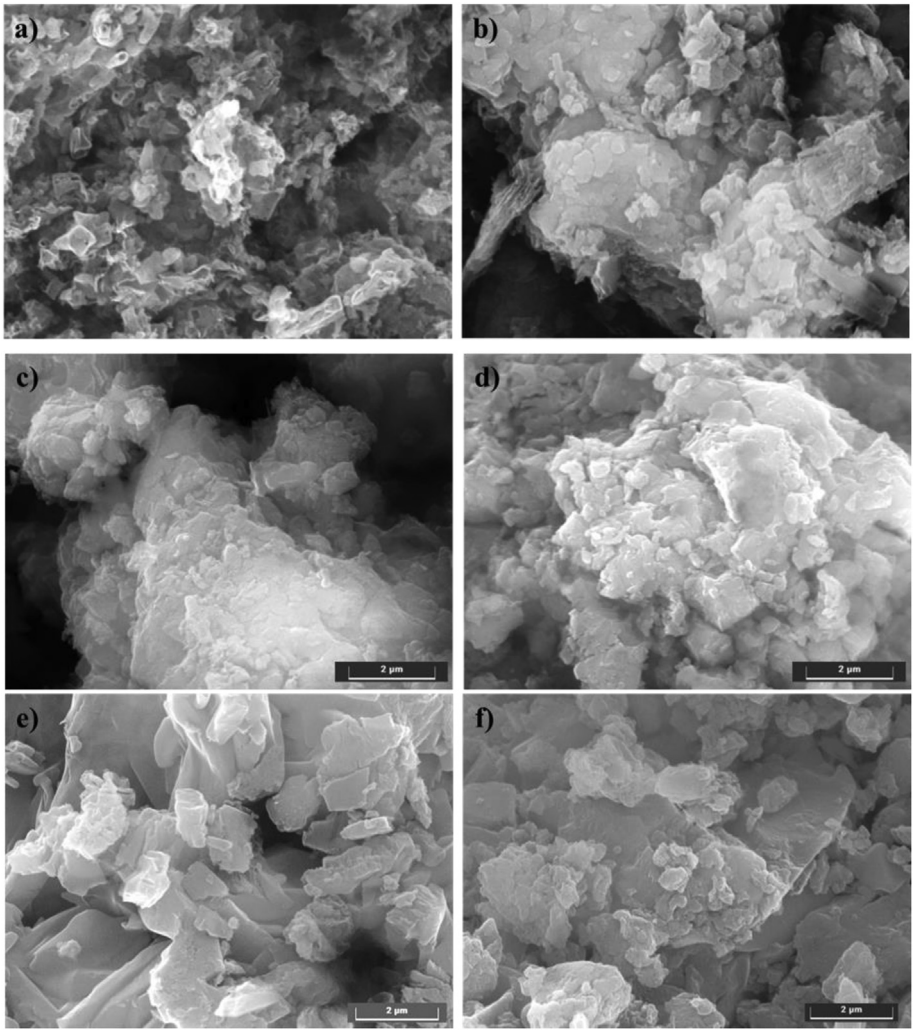

Fig. 2 – SEM images of the samples prepared from urea: a) UR-CN, b) UR20-PCN, c) DCDA-CN, d) DCDA20-PCN, e) GUA-CN, f) GUA20-PCN.

lowest thermal stability of UR, considering the same decomposition behavior of HCCP in all mixtures. The overrepresentation of phosphorus in the final materials tends to decrease with the initial content of HCCP in the mixture and by the CN precursor in the row UR >> GUA > DCDA (compare $P_{content}/P_T$ in Table 2). The decrease in the $P_{content}/P_T$ ratio with an increased concentration of HCCP is most probably attributed to the competition between the reaction of HCCP with the CN precursor and the thermal decay of HCCP. The higher the ratio of HCCP in the mixture, the more decay of HCCP

Table 2 – Comparison of the theoretical phosphorus content (P_T) and phosphorus content in prepared samples ($P_{content}$).

Sample	P_T (wt%/mol%)	$P_{content}$ (wt%/mol%)	$P_{content}/P_T$ (wt%/wt%)	$P_{content}/P_T$ (mol%/mol%)
UR1-PCN	0.268/0.065	5.96/1.94	22.24	29.72
UR10-PCN	2.67/0.70	11.3/3.95	4.23	5.64
UR20-PCN	5.35/1.5	12.7/4.40	2.37	2.89
UR40-PCN	10.7/3.68	19.1/7.04	1.19	1.91
DCDA1-PCN	0.268/0.073	0.22/0.07	0.82	0.99
DCDA10-PCN	2.67/0.78	4.65/1.59	1.74	2.04
DCDA20-PCN	5.35/1.69	5.27/1.77	0.99	1.04
DCDA40-PCN	10.7/4.05	6.07/2.05	0.57	0.51
GUA1-PCN	0.268/0.075	0.50/0.16	1.87	2.15
GUA10-PCN	2.67/0.81	3.90/1.30	1.46	1.62
GUA20-PCN	5.35/1.74	7.00/2.39	1.31	1.37
GUA40-PCN	10.7/4.16	8.30/2.79	0.78	0.67

Table 3 – Chemical composition of the prepared samples.

Sample	C (wt%/mol%)	H (wt%/mol%)	N (wt%/mol%)	P (wt%/mol%)[a]	Cl (wt%/mol%)[a]	O (wt%/mol%)[b]
UR-CN	32.8/27.0	2.88/28.4	58.1/41.0	0.82/0.26	<0.01/<0.01	5.40/3.33
UR1-PCN	31.1/26.1	2.87/29.0	56.3/40.6	5.96/1.94	<0.01/<0.01	3.77/2.38
UR10-PCN	27.2/24.5	2.42/26.2	54.9/42.5	11.3/3.95	<0.01/<0.01	4.18/2.83
UR20-PCN	25.1/22.5	2.62/28.1	52.8/40.5	12.7/4.40	<0.01/<0.01	6.78/4.55
UR40-PCN	22.9/21.8	2.29/26.2	50.9/41.6	19.1/7.04	0.13/0.04	4.68/3.35
DCDA-CN	34.2/29.5	2.32/24.0	60.7/44.8	0.10/0.03	<0.01/<0.01	2.68/1.73
DCDA1-PCN	34.0/29.0	2.44/25.0	60.4/44.1	0.22/0.07	<0.01/<0.01	2.94/1.88
DCDA10-PCN	32.4/28.7	2.25/23.9	59.2/44.9	4.65/1.59	<0.01/<0.01	1.50/0.99
DCDA20-PCN	31.5/27.3	2.51/26.1	59.3/44.0	5.27/1.77	0.03/0.01	1.39/0.90
DCDA40-PCN	30.9/27.0	2.45/25.7	58.8/44.1	6.07/2.05	0.05/0.01	1.73/1.14
GUA-CN	33.6/27.9	2.73/27.2	59.5/42.3	0.03/0.01	0.02/<0.01	4.12/2.57
GUA1-PCN	33.0/27.7	2.66/26.8	58.8/42.3	0.50/0.16	0.01/<0.01	5.03/3.16
GUA10-PCN	31.1/26.9	2.51/26.0	57.3/42.4	3.90/1.30	<0.01/<0.01	5.19/3.36
GUA20-PCN	30.6/27.0	2.41/25.5	57.0/43.2	7.00/2.39	0.33/0.11	2.66/1.76
GUA40-PCN	30.6/26.5	2.64/27.5	57.1/42.4	8.30/2.79	0.25/0.07	1.11/0.72

[a] Determined by ED-XRFS.
[b] calculated to 100%.

occurs. Similar to the observations of yields (Fig. 1), the $P_{content}/P_T$ ratios are obviously higher for the UR samples compared to the GUA and DCDA samples. This indicates that urea is more reactive with the P–Cl bond in HCCP than GUA (whose nucleophilicity is altered because of its hydrochloride nature) and DCDA (whose nucleophilicity is altered as a result of the presence of electron withdrawing cyanide moiety).

The complete chemical composition of the samples is summarized in Table 3. Carbon, hydrogen, and nitrogen contents were obtained using elemental analysis, phosphorus and chlorine contents were analyzed using XRFS, and oxygen content was calculated as the residue up to 100%. Based on the data obtained from XRFS, the chlorine concentrations in all samples are negligible. Measurable amounts of chlorine were obtained for UR40-PCN and GUA20 (40)-PCN, with the measured Cl content in the samples DCDA20 (40)-PCN being very low (Table 3). It should be noted that in the case of the GUA samples, both HCCP and GUA (guanidine hydrochloride) can be the source of the chlorine. In the GUA20-PCN sample, the molar concentrations of chlorine reached the highest value of 0.11 mol%, which means approximately 1 chlorine atom per 900 atoms of PCN, and its minimal impact on the final structure is expected. This is consistent with our previous work focused on the doping of g-C_3N_4 with phosphorus via the thermal polymerization of the melamine + HCCP mechanical mixture, in which the complete elimination of chlorine was proved by XRFS and X-ray photoelectron spectroscopy [67].

Table 3 shows that the molar ratios of hydrogen and nitrogen appear to oscillate around a typical value for the given CN precursor (UR – N: 41 mol%, H: 27 mol%; DCDA – N: 44.5 mol%, H: 24.5 mol%; GUA – N: 42.5 mol%, H: 26 mol%). On the other hand, the molar ratio of carbon always decreases with the increased presence of phosphorus (Table 3), which is especially visible in the case of UR-samples (27.0 mol% of carbon in UR-CN vs. 21.8 mol% in UR40-PCN) and substantially less notable in other samples. The concentration of oxygen varies randomly, and samples prepared from precursors with one carbon, such as UR and GUA, appear to have higher oxygen concentrations than samples prepared from DCDA. This observation indicates that at least part of the phosphorus, in dependence on the particular CN precursor, replaces carbon in the CN structure.

The contents of phosphorus presented in a form of water leachable phosphates (P_P) and phosphorus fixed in the P–CN structure (P_F) are compared in Table 4. The content of fixed phosphorus was calculated as the difference of $P_{content}$ (Table 2) and P_P.

The presence of the $(PO_4)^{3-}$ anions clearly demonstrates the fact that not all phosphorus introduced by HCCP was firmly incorporated in the P-doped CN structure. All samples except DCDA1-PCN show a higher P_F content compared to the P_P content, which signalize the most of the phosphorus is tightly bonded to the structure. A notable difference in the P_F content can be observed from the data presented in Table 4. The data also show that the P_F values grow with the phosphorus content in the case of all samples. The highest values of P_F content were obtained in the UR-derived samples (up to 14.6 wt%), as evident in Table 4. This fact is consistent with the previously discussed reactivity between HCCP and urea and the high

Table 4 – The determined content of soluble (P_P) and fixed phosphorus (P_F).

Sample	P_F (wt%)	P_P (wt%)	Sample	P_F (wt%)	P_P (wt%)	Sample	P_F (wt%)	P_P (wt%)
UR1-PCN	5.19	0.77	DCDA1-PCN	0.10	0.12	GUA1-PCN	0.48	0.02
UR10-PCN	9.29	2.01	DCDA10-PCN	3.37	1.28	GUA10-PCN	2.61	1.29
UR20-PCN	9.52	3.18	DCDA20-PCN	3.56	1.71	GUA20-PCN	5.16	1.84
UR40-PCN	14.6	4.53	DCDA40-PCN	3.85	2.22	GUA40-PCN	6.31	1.99

weight loss of urea during the calcination of the UR + HCCP mixtures (Fig. 1). The dependency of the fixed phosphorus (P_F) molar ratio on the molar ratio of the total amount of phosphorus ($P_{content}$) is shown in Fig. 3. Unlike carbon nitrides derived from UR and GUA, the fixed phosphorus content in the DCDA-PCN samples stabilized with the increasing HCCP content in the initial mixture and remained below 4 wt% even at the highest concentrations of HCCP (Table 4 and Fig. 3). It implies that each of the CN precursors appears to have its unique capacity to fix phosphorus from HCCP in its resulting P-doped CN structure, while the rest of the phosphorus remained as weakly bonded in the form of water leachable phosphates.

3.4. *Thermal analysis*

The behavior of the pure CN precursors UR, DCDA and GUA and the mechanical mixtures of UR, DCDA and GUA with HCCP (20 wt%) was studied using thermal analysis. The mass changes of the samples during heating are compared in Fig. 4.

The TG curves pictured in Fig. 4 indicate that the mechanical mixtures of CN precursors with HCCP are less thermally stable with an on-set temperature degradation slightly above 100 °C. Weight loss in this region is caused by the HCCP decomposition that takes place at more than 100 °C as reported by Sun et al. and Osada et al. [68,69], and it is supposed that the initial reaction of CN precursors with HCCP led to the formation of a certain HCCP-CN precursor complex. Both proposed processes probably led to the elimination of HCl connected with the weight loss of the samples. Weight losses connected with the gradual polymerization of pure precursors UR, DCDA, and GUA accompanied by the elimination of NH_3/H_2O can be identified for GUA at 300 °C, for DCDA at 250 °C and for UR slightly above 150 °C. The addition of 20 wt% of HCCP

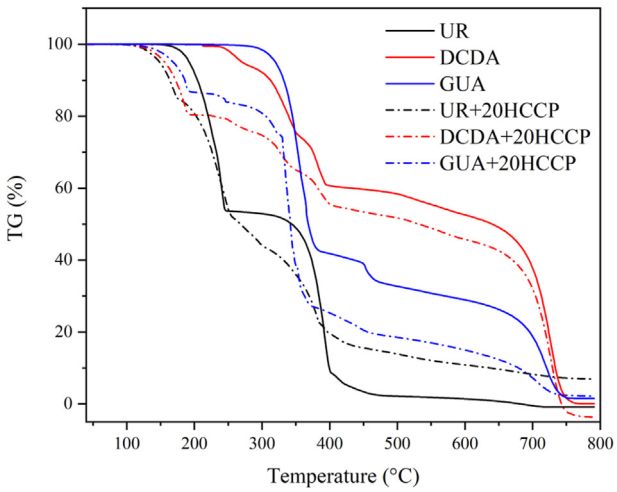

Fig. 4 – Thermally induced changes of the mass of the mechanical mixtures of studied precursors UR, DCDA, GUA and corresponding mechanical mixtures with HCCP (20 wt%).

always shifted those values to lower temperatures and made polymerization more gradual with the more complex weight loss patterns (Fig. 4).

Although the course of the TG curves is different for each mechanical mixture, the temperatures of the final weight loss for the given pure CN precursor and its mechanical mixture with HCCP are similar. The most pronounced decomposition of the samples based on the UR precursor (in Fig. 4 samples UR, UR+20HCCP) finished similarly at around 400 °C, for the samples GUA and GUA+20HCCP at around 720 °C and for the samples DCDA and DCDA+20HCCP at around 750 °C. This observation indicates an increase in the thermal stability in the order UR < GUA < DCDA. As shown in Chapter 3.1 focused

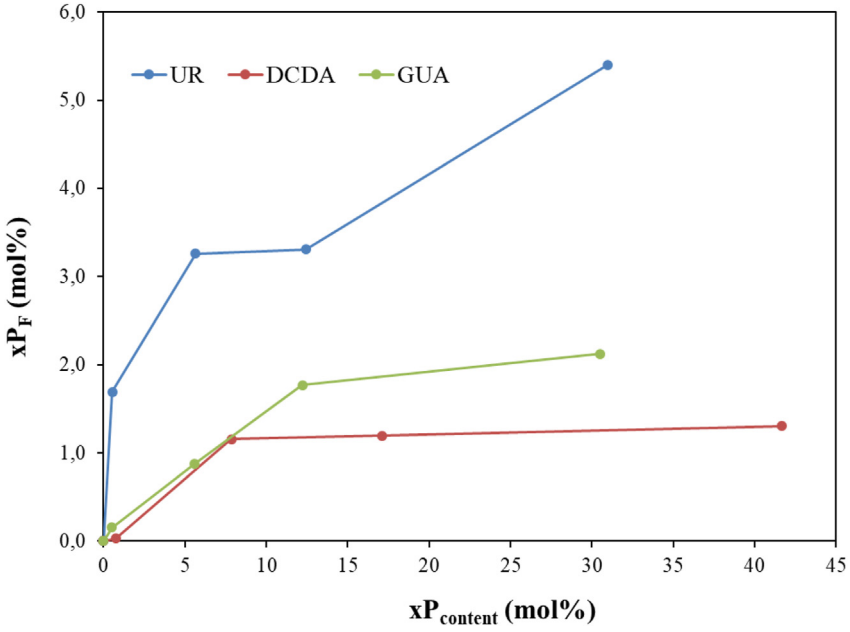

Fig. 3 – Relation between the total content of phosphorus ($xP_{content}$) and the phosphorus captured within the CN-structure (xP_F).

on the calcination yield, the highest weight loss during the calcination at 525 °C (the temperature used for the preparation of the CN samples) was observed for UR, followed by GUA, the significantly higher yield of calcination was observed for DCDA which is in good relation to the results of the TG analysis (Fig. 4).

Comparing the TG curves of the UR and UR+20HCCP samples (Fig. 4), the different course of the TG curve (different rate of weight loss) registered for the mechanical mixture UR+20HCCP in two temperature regions, indicate that the process of incorporation of phosphorus influences the reaction mechanism. The complexity of the UR transformation was recently illustrated by Kuntz et al. [70]. The authors proposed the model of UR decomposition including the formation and decomposition of eleven different species, connected with release of 6 gaseous products and comprising of two-phase changes. On the other hand, the TG curves of GUA+20HCCP and DCDA+20HCCP show similar run with the TG curves of pure GUA and DCDA.

3.5. *X-ray diffraction*

The XRD patterns of CN prepared from UR, DCDA and GUA and PCN materials prepared from these precursors are shown in Fig. 5a–c. All registered XRD patterns are dominated by two peaks with maxima at around 15 and 32° 2 Theta (CoKα), which are attributed to the (100) and (002) crystal planes of g-C_3N_4, respectively [12]. The positions of the maxima of the (002) diffraction line did not change in the case of samples prepared from UR and GUA, as evident in Fig. 5a-c. The position of the maximum of (002) diffraction line of the samples DCDA10-PCN, DCDA20-PCN and DCDA40-PCN is slightly shifted towards higher 2Theta angles (Fig. 5b), which signalizes that the incorporation of the phosphorus in the CN structure caused the decrease of the (002) interlayer space. The intensity of (002) diffraction peaks decreased with the incorporation of phosphorus, indicating the decrease in the thickness of the g-C_3N_4 particles. Similar observation was published by Li et al. [71] for spherically shaped g-C_3N_4 coupled with carbon dots.

3.6. *FTIR spectroscopy*

The FTIR spectra of the prepared materials are shown in Fig. 6a-c. The broad peak, appearing in the region of 3500 to 3000 cm^{-1}, is attributed to the stretching modes of the N–H and O–H bonds of free surface amino groups, adsorbed water, and hydroxyl species [72]. The stretching vibrations of aromatic C–N heterocycles are evidenced with characteristic bands in the region from 1635 cm^{-1} to 1250 cm^{-1} [73]. The characteristic peak with maximum at 806 cm^{-1} corresponds to the breathing vibration of the tri-s-triazine ring system

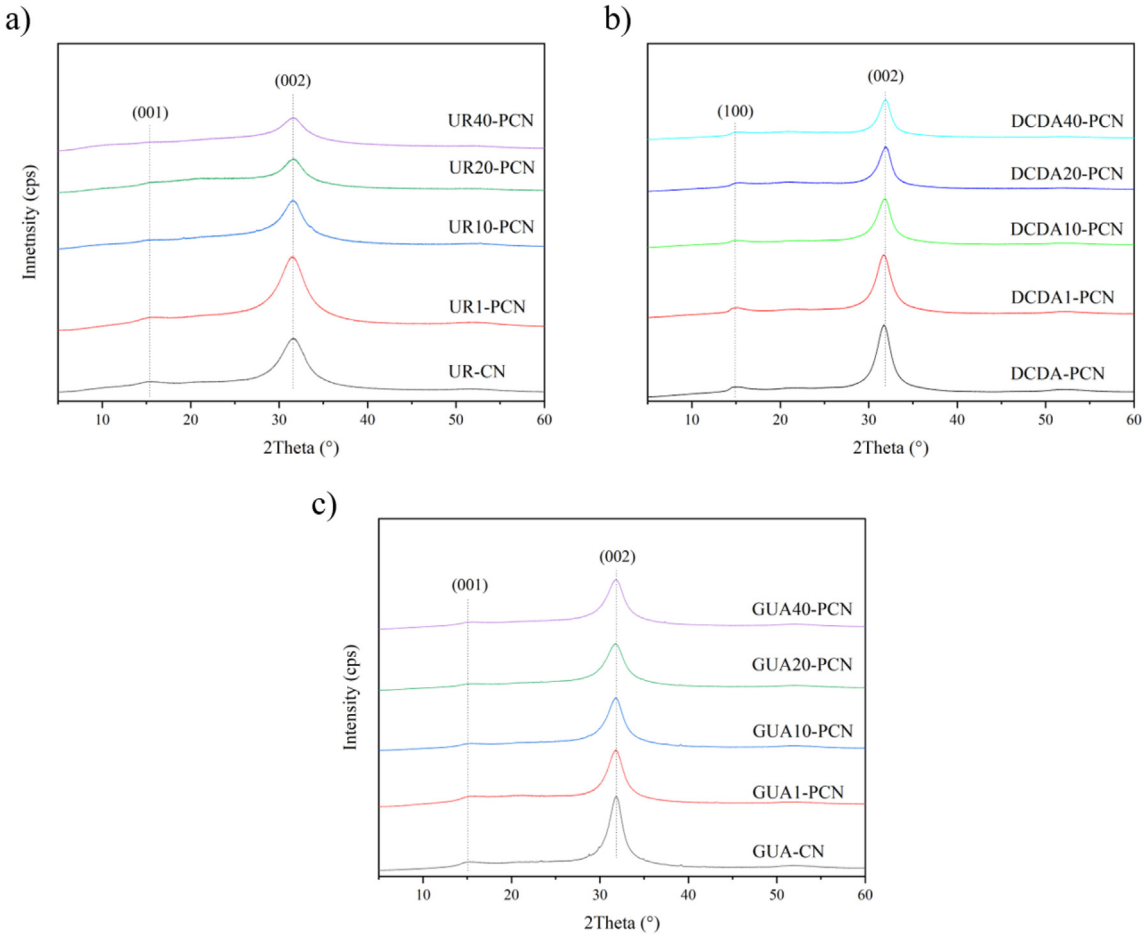

Fig. 5 – XRD patterns of UR (a), DCDA (b) and GUA (c) derived CN and PCN samples.

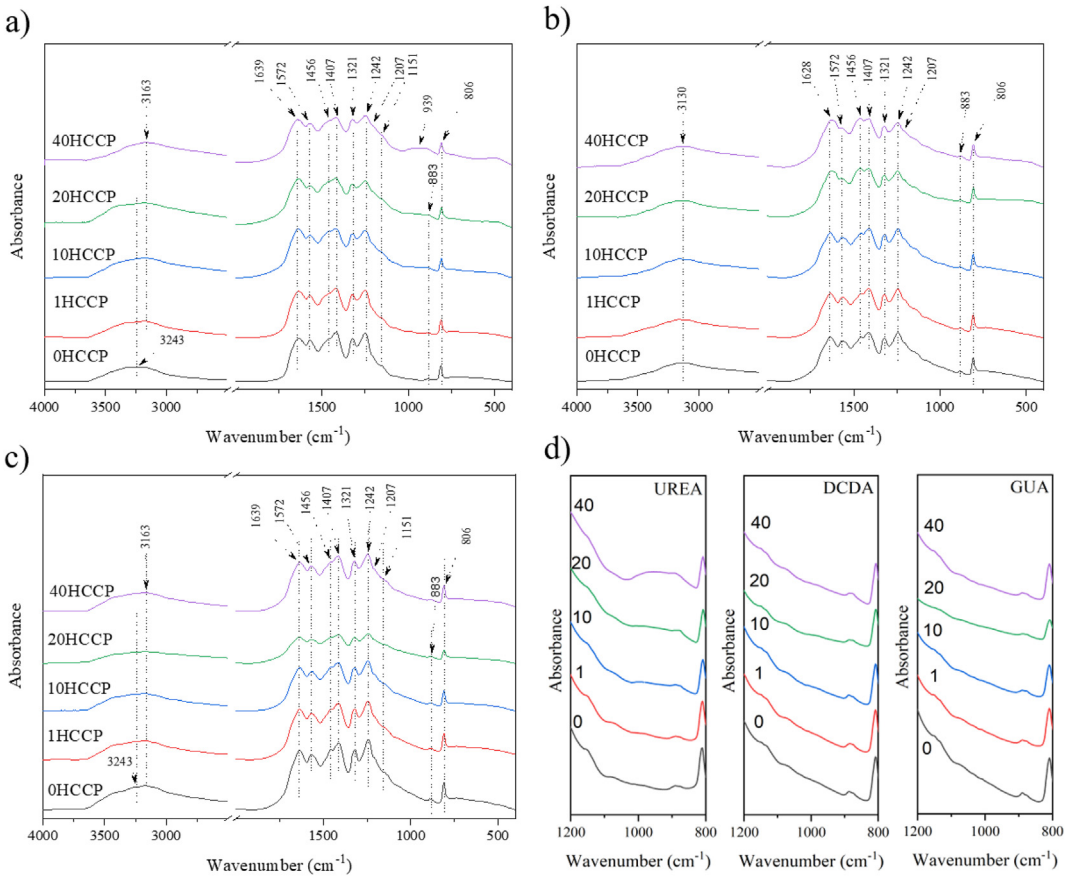

Fig. 6 – FTIR spectra of the prepared CN samples and PCN samples from the mixtures of UR + HCCP, DCDA + HCCP and GUA + HCCP calcined at 525 °C.

[74]. Comparing the spectra in Fig. 6, all of the prepared samples can be considered as graphitic carbon nitride materials.

The details of the FTIR spectra in the region of 900–1250 cm^{-1} shown in Fig. 6d did not prove the presence of P–N and P–C bonds in samples derived from DCDA and GUA mainly due to the strong absorption of the C–N heterocycle in this region. On the other hand, the sample UR40-PCN shows enhanced absorption in the 800–1000 cm^{-1} region and the respective peak could be assigned to the P–N stretching mode, indicating that the phosphorus was incorporated into the structure of CN [75]. Similarly, Li et al. [76] observed the peak at 950 cm^{-1} that indicates the presence of P–N bonds in P-doped g-C_3N_4 nanowires arrays prepared from the melamine and phosphoric acid. The chemical analysis of the synthesized samples (Table 3) proved significantly higher amount of phosphorus in the UR-derived samples and thus the presence of P–N bonds can be attributed to the process of the carbon substitution by phosphorus in the sample UR40-PCN. At the same time, the presence of P–C bonds can be excluded from the consideration. Heterocycles containing P–C or C=P–C (nitrogen substitution in the g-C_3N_4 lattice) show strong absorptions in the regions of 750–600 cm^{-1} where a set of ν(P–C) modes is usually visible [77]. This is not the case for any P-doped materials prepared within this study. Therefore, it can be concluded that there is no support on the FTIR spectra for an occurrence of P–C bonds and the nature of P-incorporation into the structure is via the substitution of carbon.

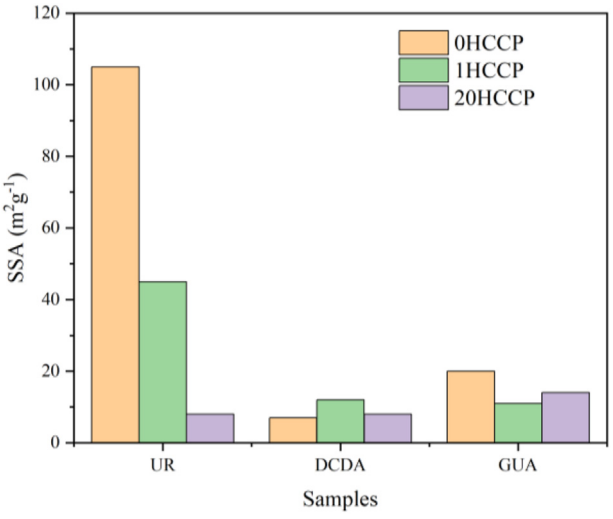

Fig. 7 – Dependency of specific surface area values on the amount of HCCP in initial calcination mixtures.

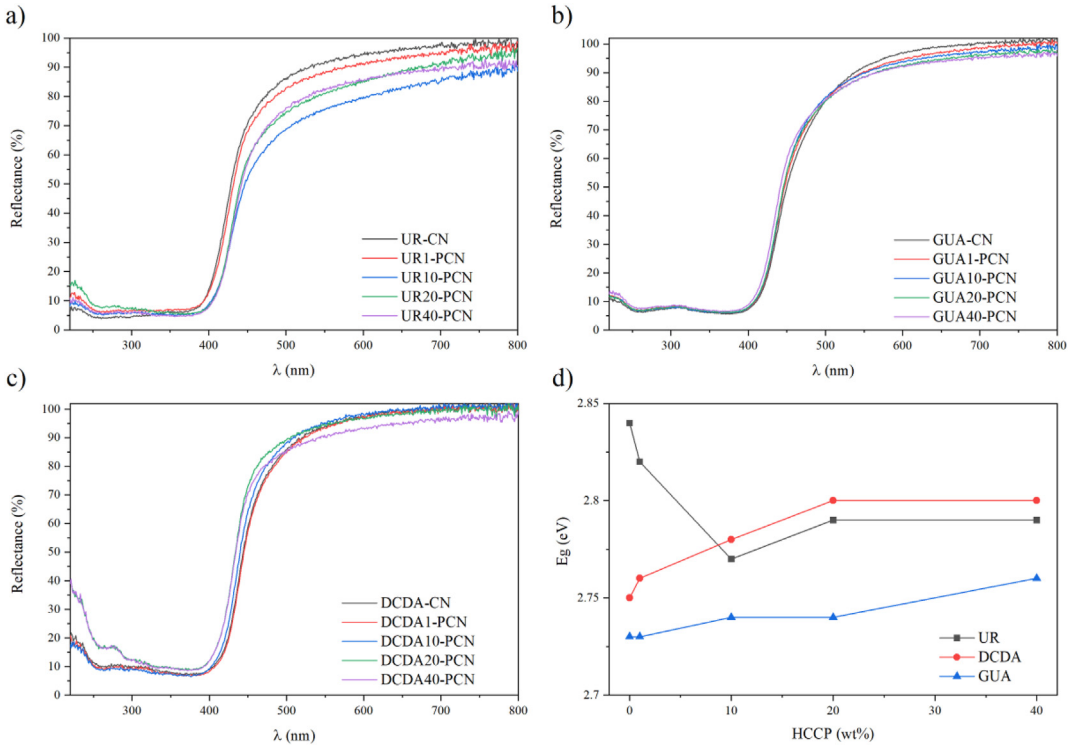

Fig. 8 – UV-VIS diffuse reflectance spectra of a) UR-derived samples, b) DCDA-derived samples, c) GUA-derived samples, and d) dependency of the band gap energies on HCCP content.

3.7. *Specific surface area*

The specific surface area values measured for the un-doped samples prepared from UR, DCDA, and GUA are compared with those values measured for selected P-doped samples in Fig. 7.

The highest SSA value of 105 m^2 g^{-1} was achieved for CN prepared from UR and the calcination of its mixture with 1 and 20 wt% of HCCP led to a pronounced decrease in this value to 45 and 8 m^2 g^{-1}, respectively, as evident in Fig. 7. This observation supports the already discussed effect of HCCP on the agglomeration of UR20-PCN particles in the part 3.2 documented by Fig. 2a) – b). Really low SSA values (below 10 m^2 g) were obtained in the case of the CN derived from the DCDA precursor. Treatment of DCDA with HCCP did not show evident effect on the SSA value (Fig. 7). In the case of samples prepared using GUA, the SSA value decreased in GUA20-PCN indicating its negative effect on this parameter.

3.8. *UV-VIS DRS spectroscopy*

The reflectance spectra of the prepared samples are shown in Fig. 8a-c, and the evaluated band gap energies (Eg) are compared in Fig. 8d.

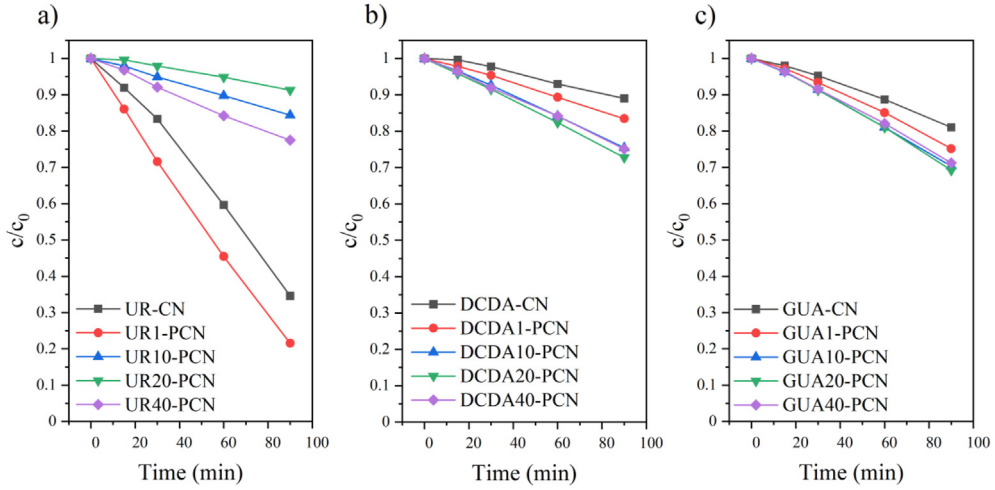

Fig. 9 – Photodegradation activity of the samples derived from UR (a), DCDA (b) and GUA (c) precursors.

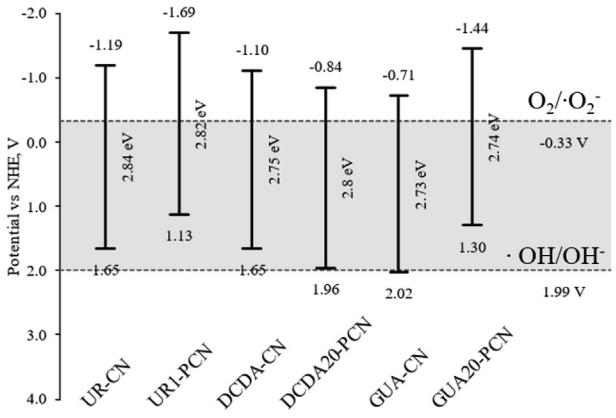

Fig. 10 – Band alignment in the selected samples.

The reflectance of the materials significantly decreased below the wavelength of 450 nm and this phenomenon is associated with the generation of photoinduced electron-hole pairs. Fig. 8d shows the effect of phosphorus on E_g of the g-C_3N_4. In the case of undoped samples, the highest E_g value was achieved for the UR-CN, the second highest value for the DCDA-CN and the lowest value for the GUA-CN. The difference between E_g of UR-CN and DCDA-CN is almost 0.1 eV. Such a high E_g value observed for the UR-CN sample is connected with the obviously higher nanosized character of the UR-CN particles causing the quantum confinement effect. The introduction of phosphorus into the UR-CN structure caused the decrease of the E_g values (Fig. 8d). The lowest E_g value within the samples of the UR-derived CN was obtained for the sample UR10-PCN and further increasing in the amount of phosphorus caused an increase in the E_g values. In the case of the samples from DCDA and GUA, a continuous increase in the E_g values was observed with the increase in the HCCP content in the calcination mixtures (phosphorus content in the resulting samples) (Fig. 8d).

3.9. *Photodegradation activity*

The changes in RhB concentration with the time of VIS light irradiation measured for the prepared samples are shown in Fig. 9. Prior to irradiation, the suspensions were magnetically stirred in the dark to reach an adsorption-desorption equilibrium. As evident from Fig. 9b-c, within the groups of the samples prepared with the DCDA and GUA precursors, the P-doped samples exhibit higher photodegradation activity than un-doped DCDA-CN and GUA-CN samples. Within the DCDA and GUA samples, the highest photodegradation activity was observed for DCDA20-PCN and GUA20-PCN samples, indicating 20 wt% of HCCP as optimal in the calcination mixtures. On the other hand, the extent of RhB photodegradation after

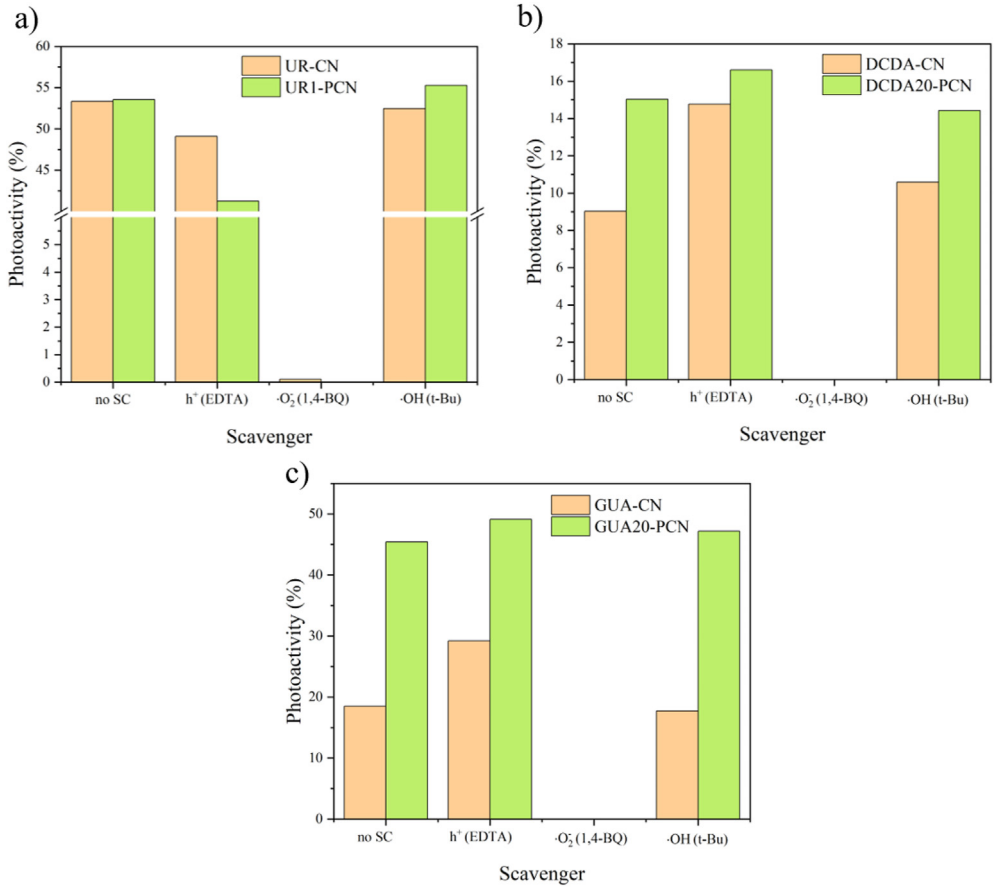

Fig. 11 – The photodegradation activity of the studied samples under 1 h long VIS irradiation in the presence of scavengers (SC).

90 min long irradiation did not exceed 32% for these samples, which was even lower activity compared to previously studied P-doped samples prepared from the MEL + HCCP mixtures [67]. A different situation was observed for the samples prepared using UR (Fig. 9a). The highest photodegradation activity showed the sample UR1-PCN, for which almost 80% of the RhB degradation was achieved within 90 min of the VIS irradiation. The second highest photodegradation activity showed the un-doped UR-CN sample. The introduction of higher phosphorus content in the UR-based P-doped samples significantly decreased the photodegradation activity, indicating the deterioration effect of phosphorus on the UR-derived P-doped CN samples photoactivity.

To assess the changes occurring at the electrochemical interface and the values of the flat band potential (V_{FB}), valence band potential (V_{VB}), and the conduction band (V_{CB}) edge potential, the Mott-Schottky technique was used (Fig. 10). This method relies on applying a bias voltage to modulate the width of space-charge interfacial double layer and, therefore, the value of capacitance when the interface's solution side can be approximated by the Helmholtz model of the double layer [78–80]. The Mott-Schottky equation (1) describes the relation between the space charge capacitance C and the applied potential V:

$$\frac{1}{C^2} = \frac{2}{\varepsilon_r \varepsilon_0 e N_D}\left(V - V_{FB} - \frac{kT}{e}\right) \quad (1)$$

where ε_r is the dielectric constant, ε_0 is the dielectric constant of vacuum, N_D is the dopant density for n-type semiconductor, T is the temperature, K is the Boltzmann constant and e is the elementary electron charge. This equation is applicable in the linear part of the plot $\frac{1}{C^2}$ vs V, where the flat band potential is an intercept of the line with the potential axis.

For n-type semiconductors, it is assumed that flat band potential is nearly identical to the conduction band (V_{CB}) edge potential according to equation (1) and (2).

$$V_{CB} \approx V_{FB(NHE)} = V_{FB} + \Delta V - 0.059 \cdot (7 - pH) \quad (2)$$

where $V_{FB(NHE)}$ is the flat band potential recalculated against NHE electrode at pH = 7, ΔV is the potential of Ag/AgCl reference electrode vs NHE. The valence band potential was calculated according to equation (3).

$$V_{FB} = V_{CB} + \frac{E_g}{e} \quad (3)$$

When the light interacts with the photocatalysts, holes are formed in the valence band, whereas electrons are transferred to the conduction band. The reactions concerning the formation of $\cdot O_2^-$ and $\cdot OH$ can be ascribed as follows (4–6).

$$OH^- + h^+ \rightarrow \cdot OH \quad (4)$$

$$O_2 + e^- \rightarrow \cdot O_2^- \quad (5)$$

$$H^+ + \cdot O_2^- \rightarrow \cdot HO_2 \quad (6)$$

The calculated energy levels are shown in Fig. 10.

Figure 10 shows that the superoxide radicals can be formed in the case of all of the samples, while hydroxyl radicals can be formed only in the case of GUA-CN. In the case of P-doped CN samples, the insertion of phosphorus into the CN structure led

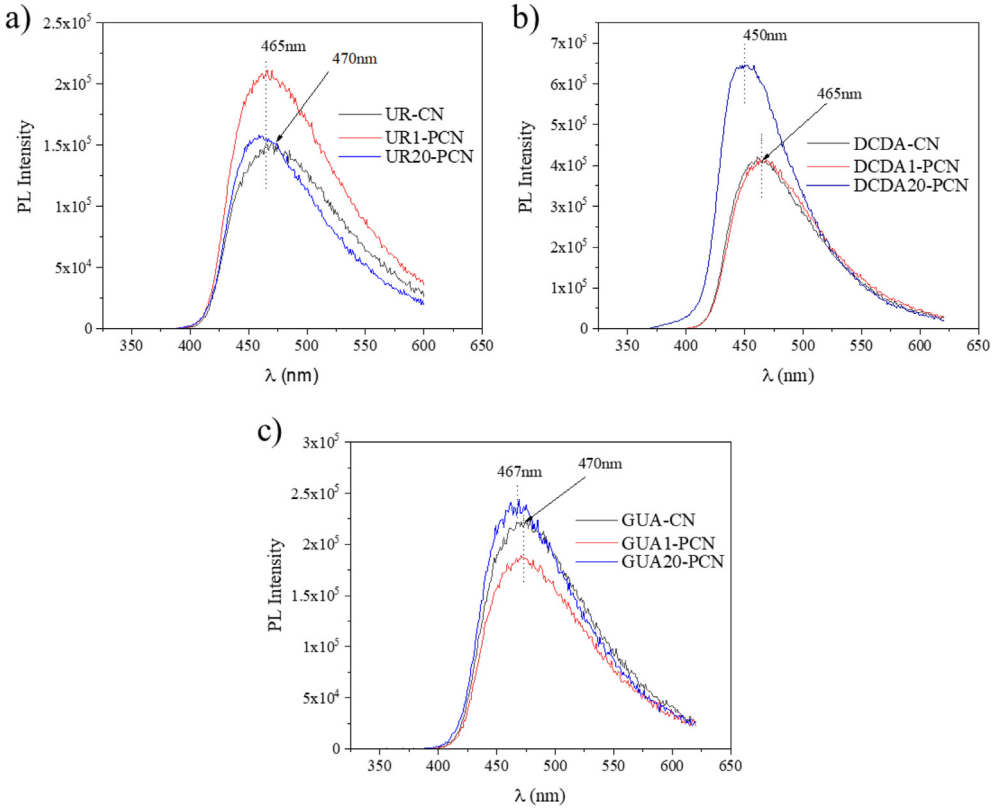

Fig. 12 – PL spectra of a) UR-derived samples, b) DCDA-derived samples, and c) GUA-derived samples.

to a decrease in the E_{VB} energy of the UR and GUA samples, and at the same time, the potential of their conduction band was also shifted to more negative values.

To confirm the effect of individual reactive species (h^+, $\bullet O_2^-$, $\bullet OH$) on RhB photodegradation, the appropriate tests were performed in the presence of their scavengers. Within these tests, EDTA was used as a holes scavenger, 1,4-BQ was used as a superoxide radicals scavenger and t-Bu was used as a hydroxyl radicals scavenger. From each of the CN precursor groups, samples showing the highest photodegradation activity were tested. The photoactivity values of the selected samples expressed as the extent of RhB degradation after 1 h long irradiation are compared in Fig. 11a-c.

In accordance with Fig. 10, Fig. 11 shows the superoxide radicals are the species responsible for the RhB photodegradation in the case of both un-doped CN and P-doped CN samples. In the case of the UR-derived samples (Fig. 11a), the photodegradation activity of the samples decreased in the presence of EDTA as the hole scavenger. In the case of the DCDA and GUA derived samples, their photoactivity increased in the presence of EDTA, whereas the same observation was reported for P-doped CN prepared by thermal polymerization of melamine in the presence of HCCP [67]. For the GUA-CN sample, the participation of hydroxyl radicals in RhB photodegradation is documented by the decrease in photodegradation activity (approximately 30%) in the presence of the t-Bu scavenger.

3.10. *Photoluminescence spectroscopy*

PL spectra of undoped UR, DCDA, and GUA and samples co-calcined with 1 and 20 wt% of HCCP are shown in Fig. 12a-c.

In the case of samples derived from UR, the highest intensity of PL signal was observed for sample UR1-PCN, as evidenced in Fig. 12a. The intensity of PL peaks is usually associated with a lower recombination rate of photogenerated carriers resulting in higher photodegradation activity as demonstrated, for example, by Zhao et al. [30]. Surprisingly, in our case, the sample UR1-PCN showed higher photodegradation activity, although it exhibited higher intensity of the maxima of PL peak intensity than the un-doped UR-CN sample. An elevated PL intensity could be related to a higher number of electron-hole pairs formation, which contributes to the increase of the number reactive radicals in aqueous suspension. This hypothesis explains the improved photodegradation activity of the sample UR1-PCN compared to the samples UR-CN and UR20-PCN (Fig. 9a), which show an almost identical value of the maximum intensity of the PL peak. The highest intensities of the PL peaks for DCDA and GUA-derived samples were obtained for HCCP content of 20 wt% (samples DCDA20-PCN and GUA20-PCN), see Fig. 12b-c. Both DCDA20-PCN and GUA20-PCN showed improved photodegradation activity, as depicted in Fig. 9b-c. As in the case of UR1-PCN, this is probably related to the formation of a higher population of electron-hole pairs. For phosphorus-doped samples derived from UR and DCDA precursors, the maxima of PL peaks (Fig. 12a-b) are blue-shifted in the spectrum. In the case of GUA-derived samples, this blue shift was observed only for the sample prepared with higher HCCP content (sample GUA20-PCN), see Fig. 12c. For g-C_3N_4 samples, this shift in the position of PL peak maxima is usually related to the quantum size effect of the nanosheet structure. Nevertheless, this is not the case with our phosphorus-doped samples, where the specific surface area values decreased after the doping process

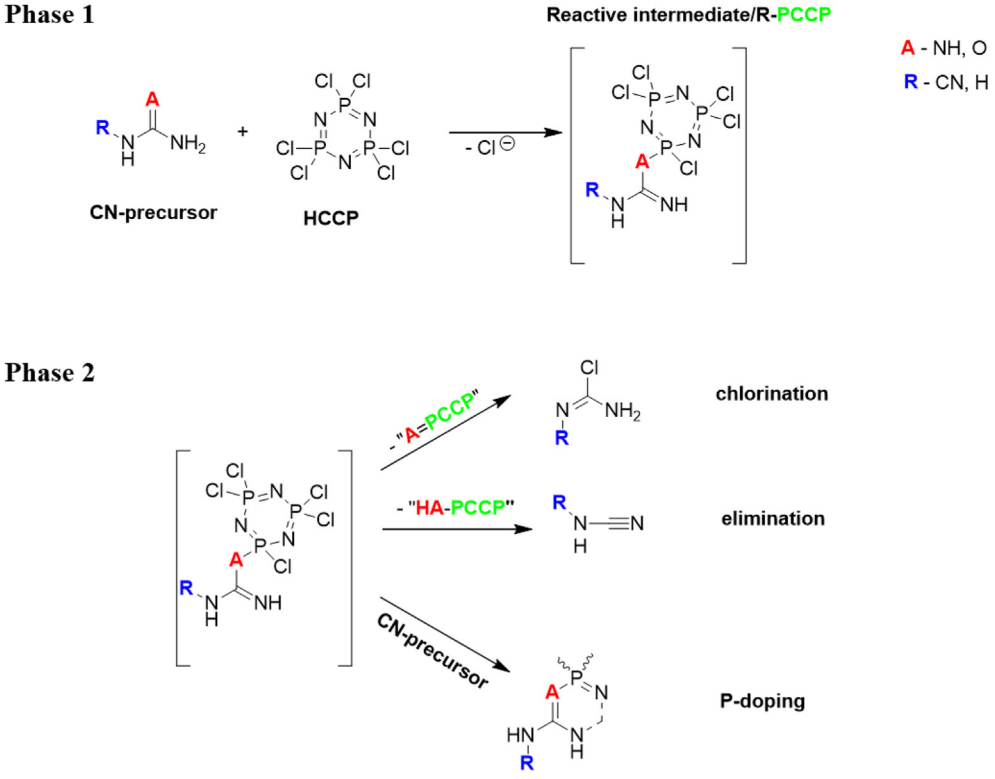

Scheme 1 – Proposal of general pathways during the CN precursors interaction with HCCP.

(UR-derived samples) or remained almost unchanged (DCDA and GUA-derived samples), see Fig. 7. Therefore, it can be argued that the blue shift was probably caused by the changes in the electronic structure of P-doped CN samples.

3.11. *Proposal of the P doping process*

In all three CN-precursors, phosphorus is present in two forms, either as part of the structure (P_F) or as phosphate (P_P), see Section 3.3. Based on FTIR spectra, the presence of P–C bonds in the final structure is unlikely, while the presence of P–N bonds was supported by FTIR analysis (Section 3.6).

Scheme 1 shows that the origin of P–CN proceeds in two subsequent phases. During the first phase, the CN-precursor reacts with HCCP to provide a reactive intermediate product (R-PCCP). This intermediate is undoubtedly chemically unstable under the conditions of our syntheses (525 °C, access to air). Its decomposition, phase 2 in Scheme 1, may proceed in three possible processes: intramolecular chlorination, elimination of HA-PCCP, or decomposition of the phosphazene core leading to the formation of C=N–P–N=C types of bonds in 6 membered heterocycles as evident from Scheme 1.

In our previous work [67], focusing on the melamine-based P–CN synthesized by the same procedure used in this study, the phosphorus content in the final samples was below 5 wt%. In our present work, the phosphorus content in the individual samples was significantly higher, indicating that the P-doping process is more efficient in incorporating phosphorus atoms into the final P–CN structure.

Although the reaction scheme is still simplified and it is supposed that the own P–CN formation process includes a more complex reaction pathway, its subdivision into two main phases is a reasonable approach reflecting the results of the TG analysis.

4. Conclusion

Urea, dicyandiamide, and guanidine hydrochloride were used as precursors for the preparation of phosphorus doped CN. The precursors were mechanically mixed with HCCP used as a source of phosphorus; the resulting mechanical mixtures were thermally treated at 520 °C. On the basis of the results, the following conclusions can be outlined:

- The yield of the calcination product depends on the CN precursor and the presence of HCCP. The lowest yield (3%) was achieved for samples prepared with urea serving as CN precursor, and the calcination product yield for this precursor increased with increasing amounts of HCCP up to 20 wt%, reaching a maximum level of 25%. The highest calcination product yield was achieved for the DCDA precursor (65%), followed by the GUA precursor (28%), both of which showed almost no change in yield up to 10 wt% HCCP.
- Regarding the growing enrichment of the final P–CN samples with phosphorus, the CN precursors can be ordered as follows: UR > GUA > DCDA.
- Two forms of phosphorus were found in the resulting products: phosphorus fixed in the CN structure and phosphorus in the form of phosphates.
- The fixed phosphorus substitutes the carbon in the triazine structural units of the final P–CN structure.
- The photodegradation activity of the DCDA and GUA-derived P–CN samples increased with the phosphorus content up to 20 wt% of HCCP but did not exceed 32%.
- The highest photodegradation activity (80%) was observed for P-doped CN based on urea with the lowest phosphorus content (UR1-PCN). This sample is preferable for photodegradation purposes with respect to: i) the increased photodegradation activity; ii) the low amount of HCCP used for its preparation; and iii) the increased yield of final product compared to undoped urea derived CN.
- The mechanism of incorporation of phosphorus into the final CN structure was explained as a two-phase process.

The phosphorus-doped g-C_3N_4 prepared by urea calcination in the mixture with a low content of HCCP was found to be an efficient way to improve the yield of the calcination product and its photodegradation activity.

Declaration of Competing Interest

The authors declare that they have no known competing financial interests or personal relationships that could have appeared to influence the work reported in this paper.

Acknowledgement

This work was supported by the Czech Science Foundation (project No. 19-15199 S), Ministry of Education, Youth and Sports, Czech Republic (contract no. 8F21007) through the research project cooperation between the AtomDeC Consortium (V4-Japan/JRP/2021/96/AtomDeC) by funding received from the Visegrad group(V4)-Japan 2021 2nd Joint Call on "Advanced Materials" and by VSB-TU Ostrava (Project No. SP2022/61). The authors also thank the Large Research Infrastructure ENREGAT (project No. LM2018098).

REFERENCES

[1] Inagaki M, Tsumura T, Kinumoto T, Toyoda M. Graphitic carbon nitrides (g-C3N4) with comparative discussion to carbon materials. Carbon 2019;141:580–607.
[2] Rono N, Kibet JK, Martincigh BS, Nyamori VO. A review of the current status of graphitic carbon nitride. Crit Rev Solid State Mater Sci 2021;46:189–217.
[3] Dong G, Zhang Y, Pan Q, Qiu J. A fantastic graphitic carbon nitride (g-C3N4) material: electronic structure, photocatalytic and photoelectronic properties. J Photoch Photobio C 2014;20:33–50.
[4] Qi KZ, Liu SY, Zada A. Graphitic carbon nitride, a polymer photocatalyst. J Taiwan Inst Chem E 2020;109:111–23.
[5] Ong W-J, Tan L-L, Ng YH, Yong S-T, Chai S-P. Graphitic carbon nitride (g-C3N4)-based photocatalysts for artificial photosynthesis and environmental remediation: are we a

step closer to achieving sustainability? Chem Rev 2016;116:7159–329.
[6] Liu J, Fu W, Liao Y, Fan J, Xiang Q. Recent advances in crystalline carbon nitride for photocatalysis. J Mater Sci Technol 2021;91:224–40.
[7] Liu R, Chen Z, Yao Y, Li Y, Cheema WA, Wang D, et al. Recent advancements in g-C3N4-based photocatalysts for photocatalytic CO2 reduction: a mini review. RSC Adv 2020;10:29408–18.
[8] Xavier MM, Nair PR, Mathew S. Emerging trends in sensors based on carbon nitride materials. Analyst 2019;144:1475–91.
[9] Vinoth S, Shalini Devi KS, Pandikumar A. A comprehensive review on graphitic carbon nitride based electrochemical and biosensors for environmental and healthcare applications. Trac Trends Anal Chem 2021;140:116274.
[10] Nasir MS, Yang G, Ayub I, Wang S, Wang L, Wang X, et al. Recent development in graphitic carbon nitride based photocatalysis for hydrogen generation. Appl Catal B Environ 2019;257:117855.
[11] Li Y, He R, Han P, Hou B, Peng S, Ouyang C. A new concept: volume photocatalysis for efficient H2 generation __ Using low polymeric carbon nitride as an example. Appl Catal B Environ 2020;279:119379.
[12] Ye S, Wang R, Wu M-Z, Yuan Y-P. A review on g-C3N4 for photocatalytic water splitting and CO2 reduction. Appl Surf Sci 2015;358:15–27.
[13] Angamuthu G, Jayabal E, Rengarajan V. Electrochemical performance evaluation of carbon nitride synthesized at different temperatures as an anode material for lithium-ion batteries. Ionics 2020;26:3863–73.
[14] Gonçalves R, Paiva RS, Lima TM, Paixão MW, Pereira EC. Carbon nitride/polypyrrole composite supercapacitor: boosting performance and stability. Electrochim Acta 2021;368:137570.
[15] Zhang J-r, Kan Y-s, Gu L-l, Wang C-y, Zhang Y. Graphite carbon nitride and its composites for medicine and health applications. Chem Asian J 2021;16:2003–13.
[16] Yang X, Zhao L, Wang S, Li J, Chi B. Recent progress of g-C3N4 applied in solar cells. J Materiomics 2021;7:728–41.
[17] Liu W, Li W, Li R, Lu Z, Li D, Zhang G, et al. Green oil additive g-C3N4: a feasible strategy to enhance the tribological properties of DLC film. Mater Res Express 2019;6:115036.
[18] Li S, Duan C, Li X, Shao M, Qu C, Zhang D, et al. The effect of different layered materials on the tribological properties of PTFE composites. Friction 2020;8:542–52.
[19] Praus P, Svoboda L, Ritz M, Troppová I, Šihor M, Kočí K. Graphitic carbon nitride: synthesis, characterization and photocatalytic decomposition of nitrous oxide. Mater Chem Phys 2017;193:438–46.
[20] Yan SC, Li ZS, Zou ZG. Photodegradation performance of g-C3N4 fabricated by directly heating melamine. Langmuir 2009;25:10397–401.
[21] Liang Q, Shao B, Tong S, Liu Z, Tang L, Liu Y, et al. Recent advances of melamine self-assembled graphitic carbon nitride-based materials: design, synthesis and application in energy and environment. Chem Eng J 2021;405:126951.
[22] Sattler A, Pagano S, Zeuner M, Zurawski A, Gunzelmann D, Senker J, et al. Melamine–melem adduct phases: investigating the thermal condensation of melamine. Chem Eur J 2009;15:13161–70.
[23] Dong F, Wang Z, Sun Y, Ho W-K, Zhang H. Engineering the nanoarchitecture and texture of polymeric carbon nitride semiconductor for enhanced visible light photocatalytic activity. J Colloid Interface Sci 2013;401:70–9.
[24] Thurston JH, Hunter NM, Wayment LJ, Cornell KA. Urea-derived graphitic carbon nitride (u-g-C3N4) films with highly enhanced antimicrobial and sporicidal activity. J Colloid Interface Sci 2017;505:910–8.
[25] Liu J, Zhang T, Wang Z, Dawson G, Chen W. Simple pyrolysis of urea into graphitic carbon nitride with recyclable adsorption and photocatalytic activity. J Mater Chem 2011;21:14398–401.
[26] Yang L, Liu X, Liu Z, Wang C, Liu G, Li Q, et al. Enhanced photocatalytic activity of g-C3N4 2D nanosheets through thermal exfoliation using dicyandiamide as precursor. Ceram Int 2018;44:20613–9.
[27] Cheng J, Hu Z, Lv K, Wu X, Li Q, Li Y, et al. Drastic promoting the visible photoreactivity of layered carbon nitride by polymerization of dicyandiamide at high pressure. Appl Catal B Environ 2018;232:330–9.
[28] Zhang X, Jia C, Liu J. Guanidine carbonate assisted supramolecular self-assembly for synthesizing porous g-C3N4 for enhanced photocatalytic hydrogen evolution. Int J Hydrogen Energy 2021;46:19939–47.
[29] Zhou Y, Zhang L, Liu J, Fan X, Wang B, Wang M, et al. Brand new P-doped g-C3N4: enhanced photocatalytic activity for H2 evolution and Rhodamine B degradation under visible light. J Mater Chem 2015;3:3862–7.
[30] Zhao K, Khan I, Qi KZ, Liu Y, Khataee A. Ionic liquid assisted preparation of phosphorus-doped g-C3N(4) photocatalyst for decomposition of emerging water pollutants. Mater Chem Phys 2020:253.
[31] Svoboda L, Praus P, Lima MJ, Sampaio MJ, Matýsek D, Ritz M, et al. Graphitic carbon nitride nanosheets as highly efficient photocatalysts for phenol degradation under high-power visible LED irradiation. Mater Res Bull 2018;100:322–32.
[32] Papailias I, Todorova N, Giannakopoulou T, Ioannidis N, Boukos N, Athanasekou CP, et al. Chemical vs thermal exfoliation of g-C3N4 for NOx removal under visible light irradiation. Appl Catal B Environ 2018;239:16–26.
[33] Pawar RC, Kang S, Han H, Choi H, Lee CS. In situ reduction and exfoliation of g-C3N4 nanosheets with copious active sites via a thermal approach for effective water splitting. Catal Sci Technol 2019;9:1004–12.
[34] Yan J, Han X, Qian J, Liu J, Dong X, Xi F. Preparation of 2D graphitic carbon nitride nanosheets by a green exfoliation approach and the enhanced photocatalytic performance. J Mater Sci 2017;52:13091–102.
[35] Yin J-T, Li Z, Cai Y, Zhang Q-F, Chen W. Ultrathin graphitic carbon nitride nanosheets with remarkable photocatalytic hydrogen production under visible LED irradiation. Chem Commun 2017;53:9430–3.
[36] Štengl V, Henych J, Slušná M, Ecorchard P. Ultrasound exfoliation of inorganic analogues of graphene. Nanoscale Res Lett 2014;9:167.
[37] Jiang L, Yuan X, Pan Y, Liang J, Zeng G, Wu Z, et al. Doping of graphitic carbon nitride for photocatalysis: a reveiw. Appl Catal B Environ 2017;217:388–406.
[38] Bai YH, Zheng YJ, Wang Z, Hong Q, Liu SQ, Shen YF, et al. Metal-doped carbon nitrides: synthesis, structure and applications. New J Chem 2021;45:11876–92.
[39] Starukh H, Praus P. Doping of graphitic carbon nitride with non-metal elements and its applications in photocatalysis. Catalysts 2020;10.
[40] Ma X, Lv Y, Xu J, Liu Y, Zhang R, Zhu Y. A strategy of enhancing the photoactivity of g-C3N4 via doping of nonmetal elements: a first-principles study. J Phys Chem C 2012;116:23485–93.
[41] Qi KZ, Liu SY, Selyaraj R, Wang W, Yan ZX. Comparison of Pt and Ag as co-catalyst on g-C3N4 for improving photocatalytic activity: experimental and DFT studies. Desalination Water Treat 2019;153:244–52.
[42] Qi KZ, Li Y, Xie YB, Liu SY, Zheng K, Chen Z, et al. Ag loading enhanced photocatalytic activity of g-C3N4 porous

nanosheets for decomposition of organic pollutants. Front Chem 2019;7.
[43] Li Y-Y, Zhou B-X, Zhang H-W, Huang T, Wang Y-M, Huang W-Q, et al. A host–guest self-assembly strategy to enhance π-electron densities in ultrathin porous carbon nitride nanocages toward highly efficient hydrogen evolution. Chem Eng J 2022;430:132880.
[44] Li B, Fang Q, Si Y, Huang T, Huang W-Q, Hu W, et al. Ultra-thin tubular graphitic carbon Nitride-Carbon Dot lateral heterostructures: one-Step synthesis and highly efficient catalytic hydrogen generation. Chem Eng J 2020;397:125470.
[45] Li Y-Y, Zhou B-X, Zhang H-W, Ma S-F, Huang W-Q, Peng W, et al. Doping-induced enhancement of crystallinity in polymeric carbon nitride nanosheets to improve their visible-light photocatalytic activity. Nanoscale 2019;11:6876–85.
[46] Matějka V, Šihor M, Reli M, Martaus A, Kočí K, Kormunda M, et al. Composites g-C3N4 and BiOIO3 for photocatalytic decomposition of N2O. Mater Sci Semicond Process 2019;100:113–22.
[47] Nemiwal M, Zhang TC, Kumar D. Recent progress in g-C3N4, TiO2 and ZnO based photocatalysts for dye degradation: strategies to improve photocatalytic activity. Sci Total Environ 2021;767:144896.
[48] Zhu Y, Li E, Zhao H, Shen S, Wang J, Lv Z, et al. Carbon nitride derived carbon and nitrogen Co-doped CdS for stable photocatalytic hydrogen evolution. Surface Interfac 2021;25:101262.
[49] Qi KZ, Lv WX, Khan I, Liu SY. Photocatalytic H-2 generation via CoP quantum-dot-modified g-C(3)N(4) synthesized by electroless plating. Chin J Catal 2020;41:114–21.
[50] Kesarla MK, Fuentez-Torres MO, Alcudia-Ramos MA, Ortiz-Chi F, Espinosa-González CG, Aleman M, et al. Synthesis of g-C3N4/N-doped CeO2 composite for photocatalytic degradation of an herbicide. J Mater Res Technol 2019;8:1628–35.
[51] Hu X, Shu Z, Guo H, Zhou J, Li T, Tan Y, et al. Metakaolin-based nano-structuring of polymeric carbon nitride and synchronous composite construction for superior photocatalytic H2 evolution. Appl Clay Sci 2020;184:105320.
[52] Wang X, Zhao Z, Shu Z, Chen Y, Zhou J, Li T, et al. One-pot synthesis of metakaolin/g-C3N4 composite for improved visible-light photocatalytic H2 evolution. Appl Clay Sci 2018;166:80–7.
[53] Wang A, Lee C, Bian H, Li Z, Zhan Y, He J, et al. Synthesis of g-C3N4/silica gels for white-light-emitting devices. Part Part Syst Char 2017;34:1600258.
[54] Wadhai S, Jadhav Y, Thakur P. Synthesis of metal-free phosphorus doped graphitic carbon nitride-P25 (TiO2) composite: characterization, cyclic voltammetry and photocatalytic hydrogen evolution. Sol Energy Mater Sol Cells 2021;223:110958.
[55] Kondo K, Murakami N, Ye C, Tsubota T, Ohno T. Development of highly efficient sulfur-doped TiO2 photocatalysts hybridized with graphitic carbon nitride. Appl Catal B Environ 2013;142:362–7.
[56] Qi KZ, Cui N, Zhang MJ, Ma YH, Wang GZ, Zhao Z, et al. Ionic liquid-assisted synthesis of porous boron-doped graphitic carbon nitride for photocatalytic hydrogen production. Chemosphere 2021:272.
[57] Chai B, Yan J, Wang C, Ren Z, Zhu Y. Enhanced visible light photocatalytic degradation of Rhodamine B over phosphorus doped graphitic carbon nitride. Appl Surf Sci 2017;391:376–83.
[58] Mahvelati-Shamsabadi T, Lee B-K. Photocatalytic H2 evolution and CO2 reduction over phosphorus-doped g-C3N4 nanostructures: electronic, Optical, and Surface properties. Renew Sustain Energy Rev 2020;130:109957.
[59] Li B, Si Y, Zhou B-X, Fang Q, Li Y-Y, Huang W-Q, et al. Doping-induced hydrogen-bond engineering in polymeric carbon nitride to significantly boost the photocatalytic H2 evolution performance. ACS Appl Mater Interfaces 2019;11:17341–9.
[60] Bellardita M, García-López EI, Marcì G, Krivtsov I, García JR, Palmisano L. Selective photocatalytic oxidation of aromatic alcohols in water by using P-doped g-C3N4. Appl Catal B Environ 2018;220:222–33.
[61] Hu S, Ma L, You J, Li F, Fan Z, Wang F, et al. A simple and efficient method to prepare a phosphorus modified g-C3N4 visible light photocatalyst. RSC Adv 2014;4:21657–63.
[62] Fang H-B, Zhang X-H, Wu J, Li N, Zheng Y-Z, Tao X. Fragmented phosphorus-doped graphitic carbon nitride nanoflakes with broad sub-bandgap absorption for highly efficient visible-light photocatalytic hydrogen evolution. Appl Catal B Environ 2018;225:397–405.
[63] Yang H, Zhou Y, Wang Y, Hu S, Wang B, Liao Q, et al. Three-dimensional flower-like phosphorus-doped g-C3N4 with a high surface area for visible-light photocatalytic hydrogen evolution. J Mater Chem 2018;6:16485–94.
[64] Deng Y, Tang L, Zeng G, Zhu Z, Yan M, Zhou Y, et al. Insight into highly efficient simultaneous photocatalytic removal of Cr(VI) and 2,4-diclorophenol under visible light irradiation by phosphorus doped porous ultrathin g-C3N4 nanosheets from aqueous media: performance and reaction mechanism. Appl Catal B Environ 2017;203:343–54.
[65] Lan D-H, Wang H-T, Chen L, Au C-T, Yin S-F. Phosphorous-modified bulk graphitic carbon nitride: facile preparation and application as an acid-base bifunctional and efficient catalyst for CO2 cycloaddition with epoxides. Carbon 2016;100:81–9.
[66] Hu C, Hung W-Z, Wang M-S, Lu P-J. Phosphorus and sulfur codoped g-C3N4 as an efficient metal-free photocatalyst. Carbon 2018;127:374–83.
[67] Škuta R, Matějka V, Foniok K, Smýkalová A, Cvejn D, Gabor R, et al. On P-doping of graphitic carbon nitride with hexachlorotriphosphazene as a source of phosphorus. Appl Surf Sci 2021;552:149490.
[68] Sun J, Gu X, Zhang S, Coquelle M, Bourbigot S, Duquesne S, et al. Improving the flame retardancy of polyamide 6 by incorporating hexachlorocyclotriphosphazene modified MWNT. Polym Adv Technol 2014;25:1099–107.
[69] Osada Y, Hashidzume M, Tsuchida E, Bell AT. Polymerization of phosphazene crystal by plasma-exposure. Nature 1980;286:693–4.
[70] Kuntz C, Kuhn C, Weickenmeier H, Tischer S, Börnhorst M, Deutschmann O. Kinetic modeling and simulation of high-temperature by-product formation from urea decomposition. Chem Eng Sci 2021;246:116876.
[71] Li B, Peng W, Zhang J, Lian J-C, Huang T, Cheng N, et al. High-throughput one-photon excitation pathway in 0D/3D heterojunctions for visible-light driven hydrogen evolution. Adv Funct Mater 2021;31:2100816.
[72] Dong G, Ai Z, Zhang L. Efficient anoxic pollutant removal with oxygen functionalized graphitic carbon nitride under visible light. RSC Adv 2014;4:5553–60.
[73] Pan H, Zhang H, Liu H, Chen L. Interstitial boron doping effects on the electronic and magnetic properties of graphitic carbon nitride materials. Solid State Commun 2015;203:35–40.
[74] Han Q, Hu C, Zhao F, Zhang Z, Chen N, Qu L. One-step preparation of iodine-doped graphitic carbon nitride nanosheets as efficient photocatalysts for visible light water splitting. J Mater Chem 2015;3:4612–9.
[75] Zhang Y, Mori T, Ye J, Antonietti M. Phosphorus-doped carbon nitride solid: enhanced electrical conductivity and photocurrent generation. J Am Chem Soc 2010;132:6294–5.

[76] Li B, Si Y, Fang Q, Shi Y, Huang W-Q, Hu W, et al. Hierarchical self-assembly of well-defined louver-like P-doped carbon nitride nanowire arrays with highly efficient hydrogen evolution. Nano-Micro Lett 2020;12:52.
[77] Thomas LC, Chittenden RA. Characteristic infra-red absorption frequencies of organophosphorus compounds—V: phosph-orus—carbon bonds. Spectrochim Acta 1965;21:1905–14.
[78] Baumanis C, Bahnemann DW. TiO2 thin film electrodes: correlation between photocatalytic activity and electrochemical properties. J Phys Chem C 2008;112:19097–101.
[79] Beranek R. (Photo)electrochemical methods for the determination of the band edge positions of TiO_2-based nanomaterials. Adv. Phys Chem 2011;2011:786759.
[80] Hankin A, Bedoya-Lora FE, Alexander JC, Regoutz A, Kelsall GH. Flat band potential determination: avoiding the pitfalls. J Mater Chem 2019;7:26162–76.